ORIGINAL ARTICLE

Superior supercapacitance behavior of oxygen self-doped carbon nanospheres: a conversion of *Allium cepa* peel to energy storage system

Gomaa A. M. Ali [1,2] · S. Supriya [3,4] · Kwok Feng Chong [1] · Essam R. Shaaban [5] · H. Algarni [6,7] · T. Maiyalagan [8] · Gurumurthy Hegde [3] (iD)

Abstract

Mesoporous carbon nanospheres are produced from biowaste, *Allium cepa* peels, well known as "onion" dry peels using the catalyst-free pyrolysis method. The synthesis process involves an unusable bio-precursor that is accumulated in millions of tons per year. The obtained materials show nanosphere morphology with particles size of 63–66 nm and surface area up to 2962 m^2 g^{-1}. After pyrolysis at 800, 900, and 1000 °C, the carbon nanospheres are directly applied for supercapacitance study without further activation processes. The electrochemical studies show promising results such as high electrode capacitance of 189.4 at 0.1 A g^{-1} in 3 M KOH. Moreover, full cell symmetrical supercapacitor is fabricated and further investigated under a wide potential window up to 1.6 V. An excellent electrochemical behavior is observed for the supercapacitor in terms of high energy density of 22.1 Wh kg^{-1} at a power density of 39.6 W kg^{-1}, high cyclic stability of 78%, and high coulombic efficiency of 90% over 4500 cycles at 0.5 A g^{-1}. These studies support carbon nanospheres obtained from *Allium cepa* wastes to be used as promising materials for supercapacitor application.

Keywords Supercapacitor · Onion peel · Agricultural waste · Carbon nanospheres · Specific capacitance

1 Introduction

The exponential growth of human population and its ever increased dependency on energy appliances have accelerated consumption of energy at an alarming rate. Therefore, the development of novel energy storage devices has become extremely necessary. Moreover, it is important to satisfy the demands of society in terms of clean, renewable, cost-effective, and environmentally benign energy sources [1, 2]. Among the various energy storage systems, supercapacitors are considered as potential candidates. In this regard, supercapacitors are approached by the global research community which offers a promise to meet the energy requirements of the globe with a safe and reliable performance [3, 4]. Supercapacitors stand as the superior energy storage devices that have gained enormous attention due to high stability, long-life cycle, large power density, and low maintenance cost. They also serve as a bridge between conventional batteries and high-power energy systems [5]. Their fast charge–discharge characteristics [6] and the ability to charge quickly have provided a venue for many researchers to develop materials for better supercapacitor performances.

The supercapacitors illustrate energy storage mechanism by two types of phenomena: electrical double layer capacitance (EDLC) and pseudocapacitance (PC). The EDLC electrode materials include various carbon-based materials that are capable of storing charges by physical adsorption and build reversible ion interactions at the electrode-electrolyte interface

Highlights

• Mesoporous carbon nanospheres are produced from *Allium cepa* dry peels.
• The materials have a nanosphere morphology with particles size of ~60 nm and surface area of 2962 m^2 g^{-1}.
• An excellent supercapacitor performance of the carbon nanospheres was observed.
• The materials showed a high cyclic stability of 78% and coulombic efficiency of 90% over 4500 cycles.
• Symmetric supercapacitor showed a high energy density of 22.1 Wh kg^{-1} within 1.7 V.

Gomaa A. M. Ali and Supriya S contributed equally towards the manuscript.

✉ Gurumurthy Hegde
  murthyhegde@gmail.com

Extended author information available on the last page of the article

[7–9]. Therefore, the criteria for fabricating supercapacitor carbon electrode include high chemical and mechanical stability, large surface area, and porosity.

In recent years, the carbon-based materials have been emerged as well-known materials for the fabrication of supercapacitor electrodes; the abundant availability, low-cost, high stability, and non-toxic nature facilitate them to be the ideal materials in the construction of high-density energy storage systems [10–12]. So far, different forms of carbon structures such as activated carbon, carbon nanotubes, graphene, and onion-like carbon have been exploited for supercapacitor applications [5, 13–17].

Among various forms, recently, the biomass-derived carbons have got enormous appreciation to be used as supercapacitor electrodes. This is because of their easy method of preparation like one-step pyrolysis and the exceptional properties they exhibit such as porous nature, high surface area, and good mechanical strength [8, 9, 11, 18]. In addition, the agricultural wastes naturally contain Na, K, Mg, and Ca compounds which induce porosity to carbon structures during carbonization, without any requirement of post-pyrolysis activation procedures [19]. Moreover, the carbonization of biowaste preserves nitrogen, oxygen, and sulfur in the carbon matrix that substantially facilitates the electrical conductivity of carbon [20, 21]. These features have been utilized to constitute highly efficient and economical supercapacitor electrodes. In this regard, many attempts have been made to introduce heteroatom functionalities to carbon structure post-carbonization to enhance supercapacitance performances [22, 23]. But such electrodes are found not so stable and result in capacitance fading. Besides, they also develop internal resistance and current leakage. Therefore, usage of carbon nanomaterials obtained from oxygen-rich bio-precursor is suggested as they contain a sufficient amount of oxygen in the carbon framework [24].

In the present work, *Allium cepa* (onion) dry peel waste is used as a precursor for the synthesis of oxygen self-doped carbon nanospheres. *Allium cepa* is one of the most commonly cultivated crops across the globe, produces huge waste, which if not handled properly can cause serious environmental issues. Reports mentioned that India produces > 1,500,000 tonnes of agro-waste per year [25], of which major part is onion dry peel; European Union produces > 500,000 tonnes of onion waste annually [26]. Besides the waste produced from food industries, domestic wastes add on to this number in the process of meeting demands of increasing population. Therefore, utilizing easily available *Allium cepa* peels to produce sustainable carbon nanoparticles facilitates waste remediation and boosts economical method of valorizing waste. Further, proximate analysis of onion peels has revealed the presence of ~ 80% of carbohydrate which can be good source of carbon; proteins, ash content, flavonoids constitute the rest. The precursor material possesses many groups, may be in the form of salts or derivatives that are predicted to facilitate the formation of porous carbon structures. The work involves fabrication of oxygen-rich supercapacitive carbon nanospheres (CNSs) by one-step pyrolysis under an inert atmosphere.

2 Experiment

2.1 Sample preparation

The onion peel waste was used as raw material for the synthesis of CNSs. The waste material was collected from southern part of India, washed thoroughly with water, and subsequently dried. The properly dried waste was ground into a fine powder using ~ 62-μm sieve, which was then subjected to pyrolysis at three consecutive temperatures, viz. 800, 900, and 1000 °C under nitrogen atmosphere (gas flow rate 150 mL cm^{-3}) [27]; the pyrolyzed products were coded as S1, S2, and S3, respectively. The detailed explanation of the synthesis of CNSs had been explained in our previous works for different waste precursors [28–30]. For comparison purpose, some parts of the work are repeated and shown in this manuscript wherever it is necessary.

2.2 Characterization

The CNSs thus obtained by one-pot pyrolysis technique (catalyst free) were characterized using energy-dispersive X-ray diffraction (EDS), field emission electron microscopy (FESEM), transmission electron microscopy (TEM), X-ray diffraction (XRD), Raman spectroscopy, and Brunauer–Emmett–Teller (BET) studies. The shape and size of the carbon nanostructures formed were demonstrated by FESEM (JEOL JSM-7100F) and TEM (JEOL, JSM 1230). The XRD patterns were recorded from 20 to 60° to understand the nature of CNS particles formed (PANalytical-X-Ray). The order of particle arrangement was checked by Raman spectroscopy (New Xplora Plus V1.2 multiline, HORIBA Jobin Yvon confocal Raman spectroscope). The Fourier-transform infrared spectra (FTIR) analyses were performed from 4000 to 400 cm^{-1} using PerkinElmer, Spectrum 100. X-ray photoelectron spectroscopy (XPS) analysis was carried out using Kratos Axis Ultra X-ray photoelectron spectrometer employing MgKα X-rays, hγ = 1253.6 eV. Further, the surface properties of CNSs were carried out using Brunauer–Emmett–Teller studies (BELSORP-max, Microtrac, Japan).

2.3 Electrodes fabrication and supercapacitance testing

For electrochemical characterization, the electrodes were prepared with a final composition of 90 wt.% of active material, 5 wt.% carbon black (Alfa Aesar), and 5 wt.%

PVDF (Aldrich, 60 wt.%). The mixture was casted on nickel foam (Goodfellow) and dried at 60 °C for 30 min. After drying, the coated mesh was uniaxially pressed at 5 tons and the weight of the active material was determined by a Shimadzu AUW220D, Japan microbalance. The active material mass loading of the obtained electrodes ranged from 3 to 6 mg cm^{-2}. A platinum wire was used as a counter electrode and Ag/AgCl was used as a reference electrode. All the electrochemical experiments were conducted in different electrolytes LiOH, NaOH, and KOH (3 M). A practical symmetrical supercapacitor has been made using two electrodes of the active material electrically isolated from each other by porous membrane pre-soaked with the electrolyte solution. It was then sandwiched and pressed into a coin cell design. The electrochemical data were collected using an AUTOLAB PGSTAT30, electrochemical workstation, the Netherlands equipped with frequency response analyzer. Cyclic voltammetry (CV) and galvanostatic charge/discharge (CDC) tests were performed at different scan rates and different current densities, respectively. Electrochemical impedance spectroscopy (EIS) data were collected from 50 kHz to 0.01 Hz, at open circuit potential (OCP) with AC amplitude of 10 mV.

3 Results and discussion

3.1 Structural and morphological characterizations

The valorization of waste onion peel to CNSs was carried out by pyrolysis at different temperatures (800, 900, and 1000 °C). The various characterization techniques aided to analyze the structural and morphological properties of CNSs, which manifested them to be applicable as supercapacitor electrode materials. First, the pyrolyzed materials were subjected to EDS analysis to determine purity, in terms of carbon percentage. The raw material contained ~ 55% of carbon, ~ 50% oxygen, and other elements such as sodium, magnesium, sulfur, potassium, and calcium. The pyrolysis process, where waste onion peel powder was heated at elevated temperature, facilitated removal of the elements other than carbon, resulting in carbonized products with higher carbon content. EDS results (Fig. 1) showed that S1, S2, and S3 having 84, 90, and 91% of carbon, respectively; oxygen was less than 10% and other elements in negligible values.

The TEM images (Fig. 1) were captured to confirm the formation of spherical shape and nanosize of pyrolyzed materials. The images clearly showed spherical particles well distributed over the area. Moreover, the images also gave information about the size of the particles. The sizes of CNSs produced at all temperatures lied in nanoscale,

where reduction of size was found with increment in temperature; the average size calculated for S1, S2, and S3 was 66, 65, and 63 nm, respectively.

The particle arrangement in the CNSs was demonstrated by XRD analysis. The XRD patterns of S1, S2, and S3 (Fig. 2a–c, respectively showed the occurrence of two prominent peaks at 26.5° and 44.5°, specific carbon nanostructures, which correspond to (002) and (100) lattice planes respectively) [8, 31]. Further, the narrow, sharp, and intense peaks correspond to crystalline/graphitic nature of CNSs are also formed. The other peaks observed at 2θ of 21°, 33°, 37°, and 39° could be attributed to metal carbonates. A similar pattern has been observed by Carrot et al. during the XRD analysis of the pyrolyzed product of lignin [32]. Moreover, the XRD results corroborated with Raman spectroscopic outcomes. Two major peaks appeared in Raman spectroscopic plots (Fig. 2d); a peak at 1594 cm^{-1} represented the disorder present in nanocarbon structures, whereas the peak observed at 1347 cm^{-1} indicated the formation of graphitic CNSs [33]. Thus, the above analyses confirmed the formation of pure, crystalline, and graphitic CNSs by the pyrolysis of a biowaste material.

FTIR (Fig. 2e) was carried out to investigate the bonding and thus purity of the CNS compounds. The peak at 3429 cm^{-1} is due to O–H bond stretching; the stretching frequency of C–H appeared as twin peaks at 2931 and 2848 cm^{-1}. The peak at 1572 cm^{-1} could be attributed to sp^2 hybridized carbon, C=C stretching. At 1438 and 877 cm^{-1}, bending vibrations of C–H and C=C were formed. The FTIR analysis of CNSs showed that the nanomaterials were highly pure with traces of heteroatoms like oxygen [33].

The XPS analysis was performed for carbon nanospheres synthesized at 1000 °C to demonstrate the chemical nature at the surface. The wide spectral analysis (Fig. 3a) revealed the presence of carbon and oxygen bound in different ways; also, the presence of nitrogen in minute quantity was confirmed. The XPS core-level spectra of C 1 s, O 1 s, and N 1 s are given in Fig. 3b–d, respectively. The XPS spectrum of C 1 s exhibits the intense characteristic peak at binding energy value 284.8 eV which could be attributed to C–C or C=C bonds in the carbon matrix. The other two minor peaks were formed at 285.3 and 290.0 eV. The binding energies of these small peaks were 0.5 and 5.2 eV higher than the binding energies of carbon atoms. This indicated the existence of C–O and C=O bonds in the carbon matrix [34]. Further, XPS spectrum of O 1 s in Fig. 3c showed peaks at 532.4 and 532.7 eV which could be attributed to C–O or C=O bonds in CNSs [34]. XPS analysis also showed the traces of nitrogen entities in CNSs forming nadir intensity peaks. The XPS core-level spectrum of N 1 s showed four peaks at 395.1, 398.0, 400.8, and 403.7 eV. The major peak appeared at 400.8 eV was correspondent to graphitic nitrogen substituting carbon atoms in carbon

Fig. 1 EDS plots of showing an increase in carbon percentage from S1 to S3; TEM images of S1, S2 and S3
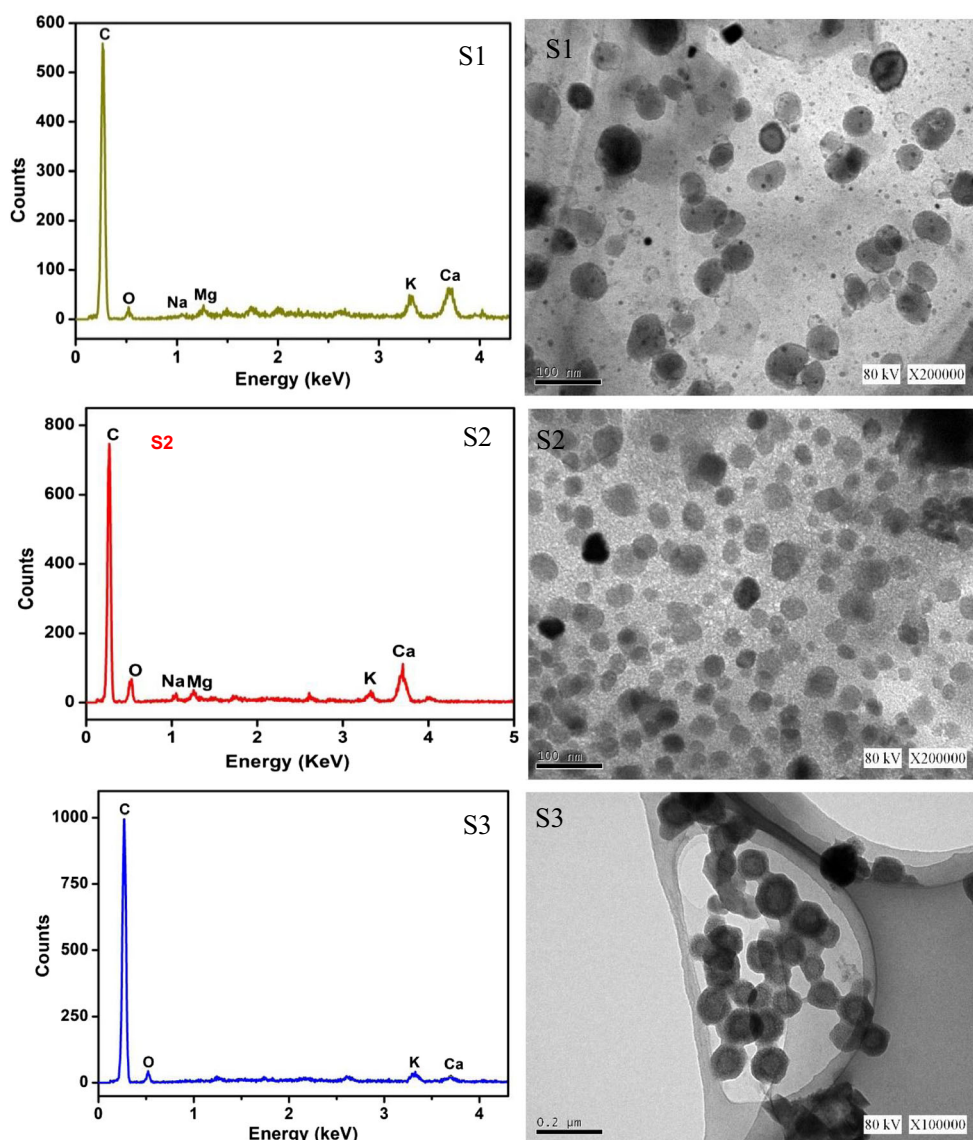
network. The peaks at 395.1 and 398.0 might be due to sp^2 nitrogen forming pyridinic nitrogen and the oxidized nitrogen produced a peak at 403.7 eV [35].

Further, the surface area study was carried out by the N_2 adsorption–desorption method to determine the surface morphological properties of CNSs. The N_2 adsorption–desorption isotherms are given in supplementary as Fig. S1. The results reveal that the isotherms can be classified according to the IUPAC as reversible type IV which characterizes a material that contains mesopores and has a high energy of adsorption [36, 37]. The investigations emphasized on surface area and porosity; of the CNS materials, S1 exhibited the lowest surface area (692 m^2 g^{-1}), whereas S3 showed the largest value (2962 m^2 g^{-1}) and S2 had 930 m^2 g^{-1}. The obtained BET surface area is higher than those reported for KOH activation of wax gourd-derived carbon materials [38]. The mesoporous CNSs were found to have a similar pattern of values with

regard to porosity. The total pore volumes of S1, S2, and S3 were found to be 0.4, 0.5, and 2.1 m^3 g^{-1} respectively. Figure 4 a shows the direct relationship between pyrolysis temperature, surface area, and total pore volume. With increase in temperature from 800 to 1000 °C, the surface area and pore volume in CNSs were also found to increase. These studies proved to be important in manifesting the CNSs for supercapacitor applications. Table 1 summarizes the textural properties analyses results along with average particle size.

Micropore volume in CNSs was determined by the volume of gas adsorbed using the t-plot method (Fig. 4b). The total micropore volumes were 0.4, 0.5, and 1.7 cm^3 g^{-1} in S1, S2, and S3, respectively. The waste onion peel derived CNSs were found to be constituted by mesopores along with micropores. The combination of these two types of pores well facilitates the diffusion of ions into void and retention of electrons, thereby producing higher capacitance.
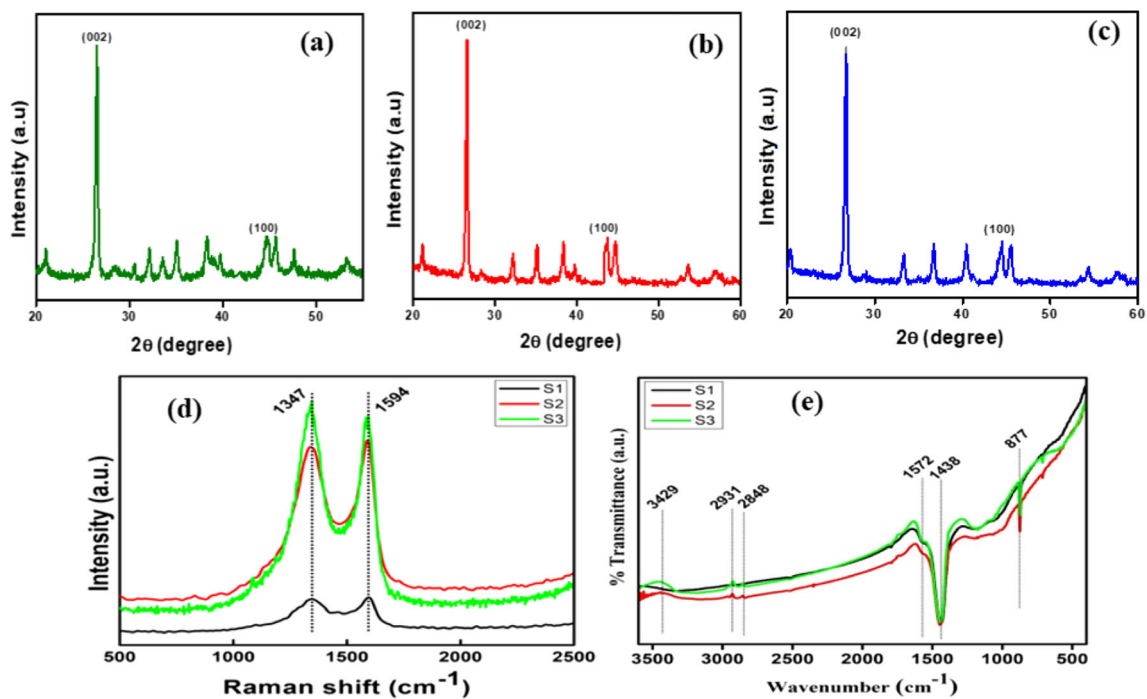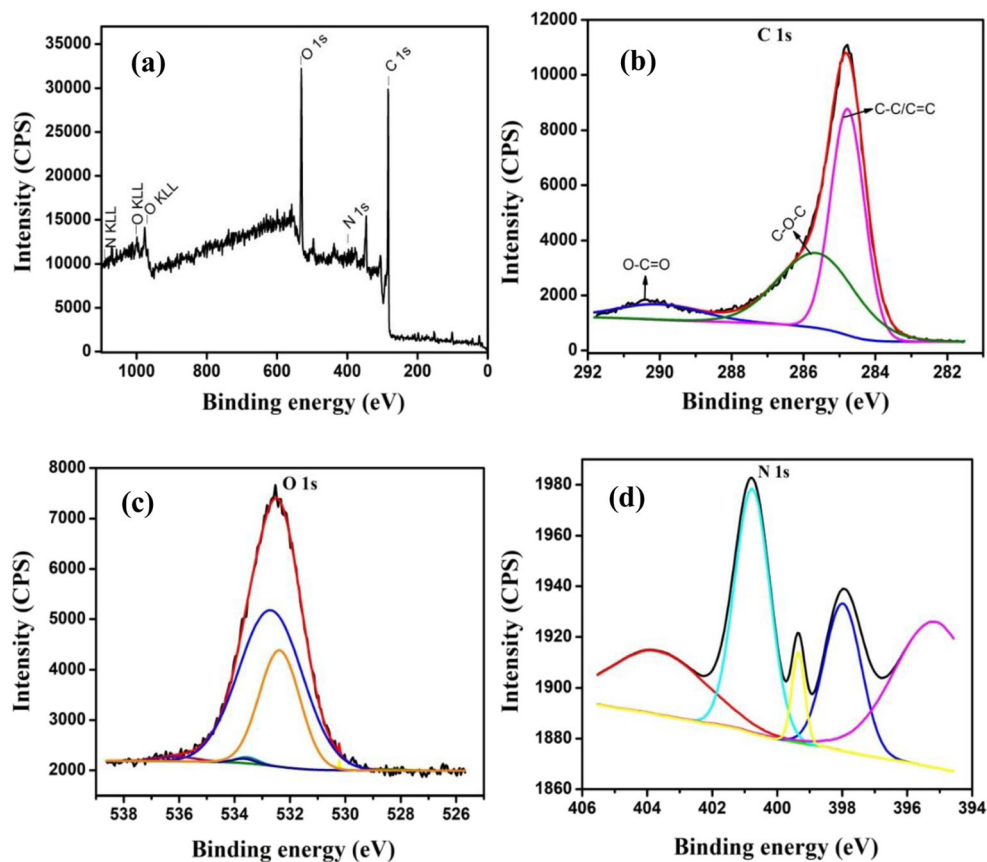
Fig. 2 XRD patterns of CNSs **a** S1, **b** S2, **c** S3, **d** Raman, and **e** FTIR spectra for S1, S2, and S3 samples

Fig. 3 XPS analysis of S3 **a** wide spectral measurement, **b** C 1 s, **c** O 1 s, and **d** N 1 s
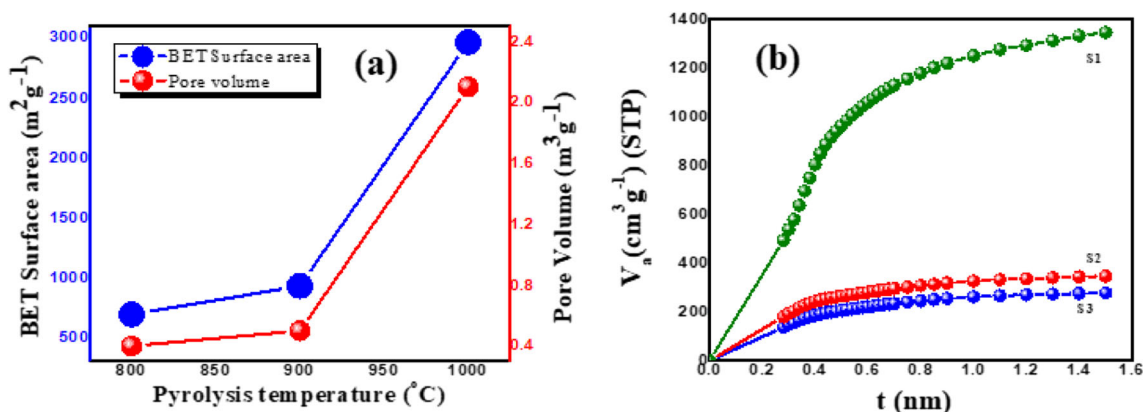
Fig. 4 **a** Surface area and pore volume as functions of pyrolysis temperature; **b** t- plots showing volume of gas adsorbed by CNSs having pore size < 2 nm

3.2 Electrochemical studies

3.2.1 Supercapacitor electrodes performance

Effect of electrolyte The electrochemical behavior and the stability of the electrodes fabricated from CNSs synthesized from *Allium cepa* peels were studied using cyclic voltammetry galvanostatic charge/discharge tests. The electrochemical performances of the electrodes were studied in different electrolytes (3 M LiOH, NaOH, and KOH) to optimize the testing conditions. The tests were performed after initial stabilization for 20 cyclic voltammetry cycles at a scan rate ranging between 5 and 100 mV s^{-1} in a potential window of − 1–0 V. Cyclic voltammetry curves measured at 50 mV s^{-1} scan rate, charge/discharge at 0.5 A g^{-1} current density, and the specific capacitance as a function of current density in different electrolytes (LiOH, NaOH, and KOH) are shown in Fig. 5a–c, respectively. Cyclic voltammetry curves exhibit almost rectangular-like shape with no obvious redox peaks, which reveals the EDLC behavior in all electrolytes. This cyclic voltammetry shape was found to be similar as presented elsewhere for activated carbon from waste *Camellia oleifera* shell [39]. In addition, the galvanostatic charge/discharge plots display nearly a straight line with a neglected iR drop, indicating a good current–voltage response. In KOH, the discharging time is higher indicating high charge accumulations. The specific capacitance (C_s)

as a function of current density calculated from the slope of charge–discharge curves according to Eq. (1) [38, 40]:

$$C_s = \frac{I}{m\,(\Delta V/\Delta t_d)} \tag{1}$$

where I is the discharge current, dV/dt is the slope of discharge curve, and m is the mass of active materials on the working electrode. The C_s was found to decrease with increasing discharge current and found to be 35.5, 88.3, and 189.4 F g^{-1} was obtained at 0.1 A g^{-1} in LiOH, NaOH and KOH, respectively. Figure 6 shows the cyclic voltammetry at different scan rates and galvanostatic charge/discharge at different current densities for S3 in LiOH, NaOH, and KOH. KOH electrolyte shows the highest specific capacitance among all electrolytes; thus, it has selected for further testing. These high specific capacitance values could be attributed to the high porosity and surface area [41] that could be accessible to the electrolyte ions. The results suggest that the capacitance in the basic electrolytes is based only on non-Faradaic electrostatic sorption of ions on the double layer [42]. On the other hand, KOH shows the highest capacitance which is due to smallest radius of hydration of K$^+$ (3.31, 3.58, and 3.82 Å for K$^+$, Na$^+$, and Li$^+$, respectively) and highest molar conductivity of K$^+$ (73.5, 50.1, and 38.6 cm^{2}Ω^{-1} Mol^{-1} for K$^+$, Na$^+$, and Li$^+$, respectively) among other electrolyte ions [43]. In addition, the deviation from linearity of the galvanostatic charge/discharge curves may be attributed to the pseudocapacitance contribution of oxygen functional groups [44], which lead to high specific capacitance values [45].

Effect of carbonization temperature To optimize the carbonization temperature, three samples annealed at different temperatures (800, 900, and 1000 °C) coded as S1, S2, and S3, respectively, were investigated. The cyclic voltammetry curves measured at 50 mV s^{-1} scan rate, charge/discharge
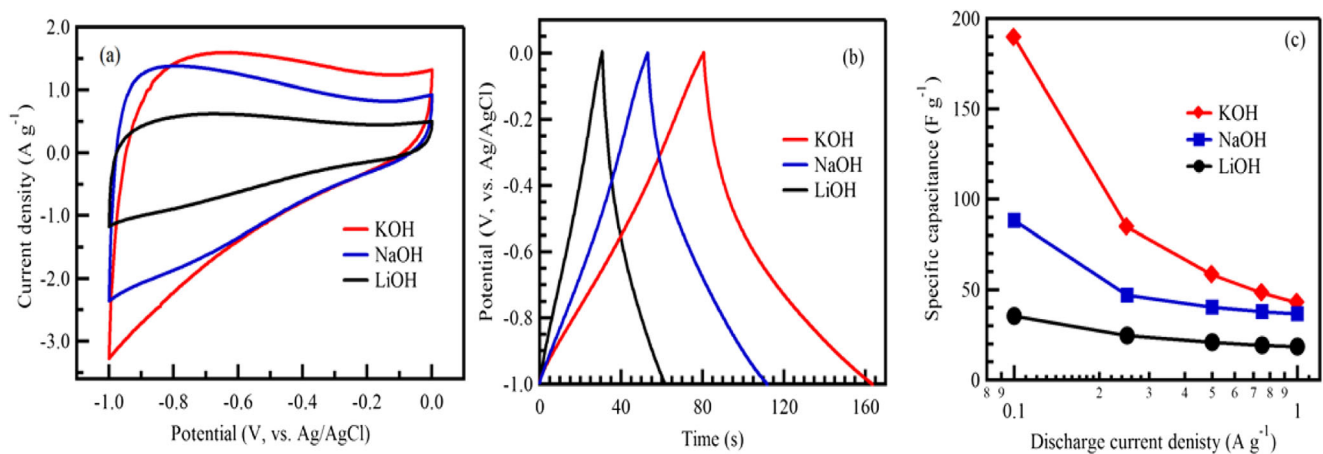
Table 1 Summarization of textural properties analyses results

CNS	BET surface area (m^2 g^{-1})	Average pore size (nm)	Pore volume (m^3 g^{-1})
S1	692	2.5	0.4
S2	930	2.3	0.5
S3	2962	2.8	2.1

Fig. 5 Cyclic voltammetry at 50 mV s^{-1} (**a**), galvanostatic charge/discharge at 0.5 A g^{-1} (**b**), and specific capacitance as a function of current density (**c**) of S3 in the indicated electrolytes

0.5 A g^{-1} current density, and the specific capacitance as a function of current density for the three different electrodes are shown in Fig. 7a–c, respectively. Cyclic voltammetry curves exhibited almost rectangular-like shape with no obvious redox peaks, which revealed the EDLC behavior in all electrolytes. In addition, the galvanostatic charge/discharge plots displayed nearly a straight line with a neglected iR drop, indicating a good current–voltage response. For S3, the discharging time

was higher indicating high charge accumulations. The calculated specific capacitance was found to decrease with increasing discharge current and found to be 68.5, 154.3, and 189.4 F g^{-1} was obtained at 0.1 A g^{-1} for S1, S2, and S3, respectively. Figure 8 shows the cyclic voltammetry at different scan rates and galvanostatic charge/discharge at different current densities for S1, S2, and S3 in KOH. S3 showed the highest specific capacitance among all materials; thus, it has selected for
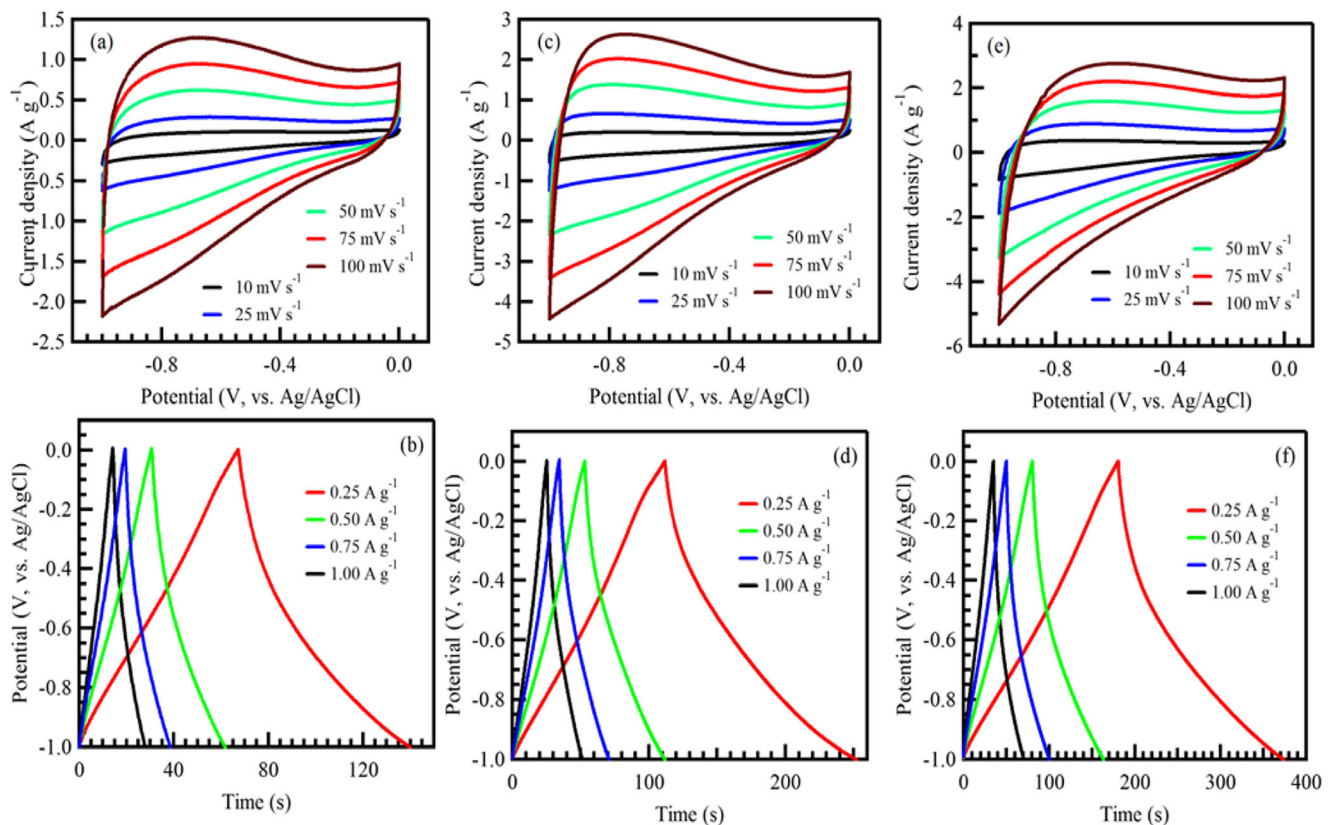

Fig. 6 Cyclic voltammetry at different scan rates and galvanostatic charge/discharge at different current densities for S3 in 3 M LiOH (**a, b**), NaOH (**c, d**), and KOH (**e, f**), respectively
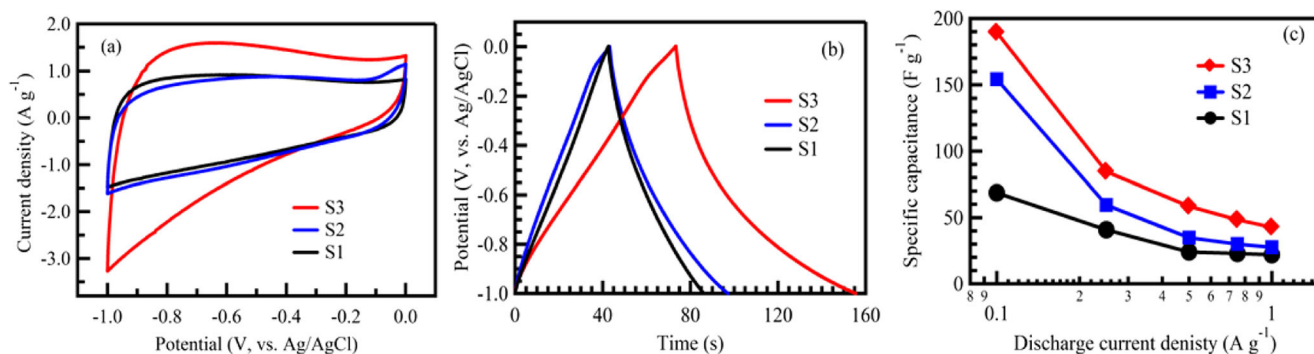
Fig. 7 Cyclic voltammetry at 50 mV s^{-1} (**a**), galvanostatic charge/discharge at 0.5 A g^{-1} (**b**), and specific capacitance as a function of current density (**c**) for the indicated materials in 3 M KOH

further testing. The findings were compared with other carbon materials as listed in Table 2.

EIS was performed to investigate the chemical and physical processes occurring on the electrode surface [17]. Nyquist plots are shown in Fig. 9a and the inset represents the high-frequency region of the recorded full impedance plot. At low-frequency region, the curve was parallel to the ordinate, indicating a better capacitive behavior in KOH. A small semi-circle in the high-frequency region and a vertically straight line in the low-frequency region could be seen clearly from the figure. R_s and R_{ct} were found to be very small, indicating high electrical

conductivity of carbon materials. The vertical linear section in the low-frequency region demonstrated a pure capacitive behavior and represented an ideal supercapacitor. The result of EIS measurement indicated that the CNSs had good capacitive performance. All fitting parameters are summarized in Table 3.

Bode plots for CNS supercapacitor materials are shown in Fig. 9b. The phase angle of S1, S2, and S3 in KOH was found to be − 75.5°, − 79.1°, and − 80.1°, respectively which was close to ideal supercapacitor (− 90°) [51, 52]. Plots of the real (C') and imaginary (C'') parts as functions of frequency (using the equation mentioned elsewhere
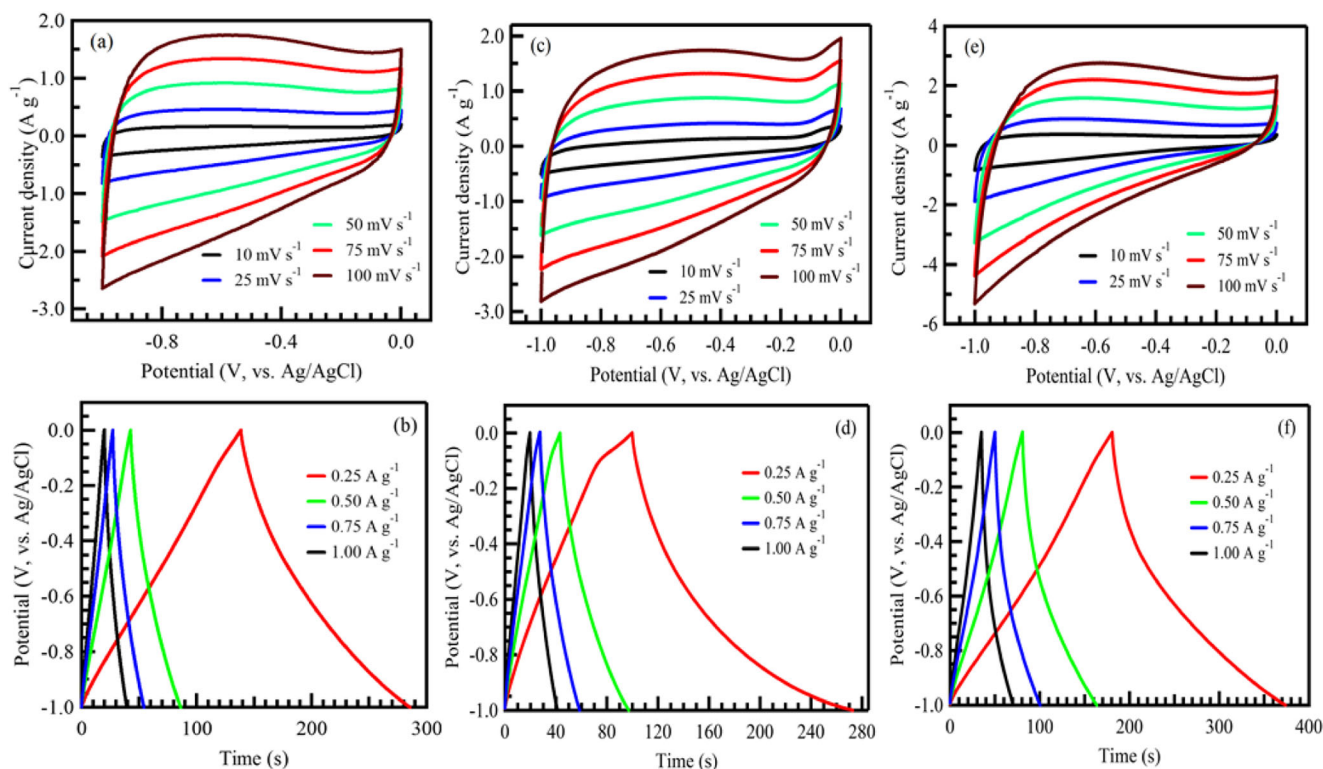

Fig. 8 Cyclic voltammetry at different scan rates and galvanostatic charge/discharge at different current densities in KOH for S1 (**a**, **b**), S2 (**c**, **d**), and S3 (**e**, **f**), respectively

Table 2 Comparison of reported specific capacitance with carbon-based materials

Carbon-based electrode	Precursor	Specific capacitance (F g^{-1})	Electrolyte	Ref.
MWCNTs-Cyst	Industrial grade MWCNTs	23 @ 0.25 A g^{-1}	1 M Na$_2$SO$_4$	[7]
MWCNTs		6 @ 0.25 A g^{-1}		
KOH-activated carbon	Fir trees	180 @ 10 mV s^{-1}	0.5 M H$_2$SO$_4$	[46]
Steam-activated carbon		110 @ 10 mV s^{-1}		
Rotten carrot-activated carbon	Rotten carrot	113.9 @ 10 mV s^{-1}	10 M EMITf in SN	[47]
Aluminum foil with a carbonaceous coating and activated carbon	Commercial activated carbon	95 @ 20 mA cm^{-2}	1.5 M NEt$_4$BF$_4$	[48]
KOH-activated recycled jute	Recycled jute	185 @ 500 mA g^{-1}	3 M KOH	[49]
Activated carbon derived from banana fibers	Banana fibers	74 @ 500 mA g^{-1}	1 M Na$_2$SO$_4$	[50]
Oxygen self-doped carbon nanospheres	Onion peel	189.4 @ 0.1 A g^{-1}	3 M KOH	This work

[40, 51]) are shown in Fig. 9c and d. In KOH, S1, S2, and S3 showed lower relaxation time of 0.62, 0.63, and 0.63 s indicating good electrochemical supercapacitive properties and fast galvanostatic charge/discharge characteristic response.

3.2.2 Practical symmetrical supercapacitor performance

The symmetric supercapacitor of S3//S3 had been fabricated and tested using cyclic voltammetry under different operating voltages. In KOH solution, it could work under

Fig. 9 Nyquist (**a**) and Bode (**b**) plots (the inset is zoomed view of the plots at high-frequency region), real (**c**), and imaginary (**d**) parts of the capacitance as functions of the frequency at OCP of the indicated materials in 3 M KOH
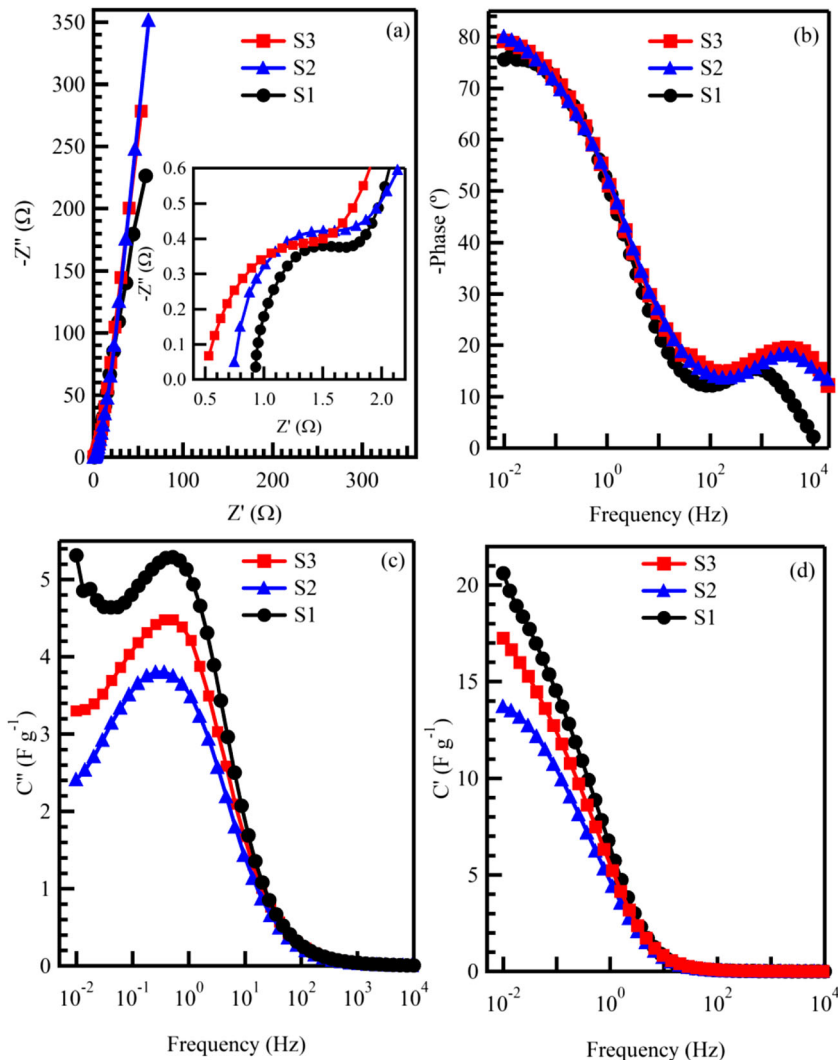
Table 3 Fitting parameters of the experimental impedance data for the electrode materials in 3 M KOH

Electrode	R_s (Ω)	R_{ct} (Ω)	C (mF)	CPE (Ω^{-1} s^n)	W (Ω)	τ (s)
S1	0.95	0.71	0.29	0.060	0.158	0.62
S2	0.80	0.78	0.11	0.051	0.077	0.63
S3	0.58	0.73	0.11	0.062	0.087	0.63

1.7 V, which indicated high energy was stored in the supercapacitor. As shown in Fig. 10 a and b, the symmetric supercapacitor shows a quasi-rectangular cyclic voltammetry curve under all potential windows and all scan rates. At a low scan rate, electrolyte ions had more time to diffuse into the pores of the S3, making the huge increase in the capacitance values. However, at higher scan rate, the electrolyte ions did not have sufficient time to diffuse, and they increased the ionic resistivity generating slower capacitance values increment [53]. The galvanostatic charge/discharge characteristics of S3//S3 supercapacitor were performed at different current densities and different voltage windows and the results are presented as shown in Fig. 10 c and d. The cell showed a linear charge and

discharge curves even under high voltage limit (1.6 V). The calculated specific capacitance decreased with increasing discharge current and the highest specific capacitance of 81.3 F g^{-1} was obtained at 0.01 A g^{-1} in 3 M KOH (Fig. 10e). The decreasing in specific capacitance with increasing current density implies the potential difference in pores because of the ohmic resistance of the electrolyte [54]. The energy (E) and power (P) densities can be calculated from CDC data using Eqs. (2) and (3), respectively [12, 38].

$$E = \frac{1}{2} C_s V^2 \tag{2}$$

$$P = \frac{E}{\Delta t_d} \tag{3}$$

The Ragone plot for S3//S3 is shown in Fig. 10f, showing the maximum energy density of 22.1 Wh kg^{-1} at a power density of 39.6 W kg^{-1}. The energy density was found to be higher than those obtained for biomass-based N-doped hierarchical porous carbon nanosheets (10.2 Wh kg^{-1}) [55], KOH activation of wax gourd-derived carbon materials (13.0 Wh kg^{-1}) [38], KOH activation of
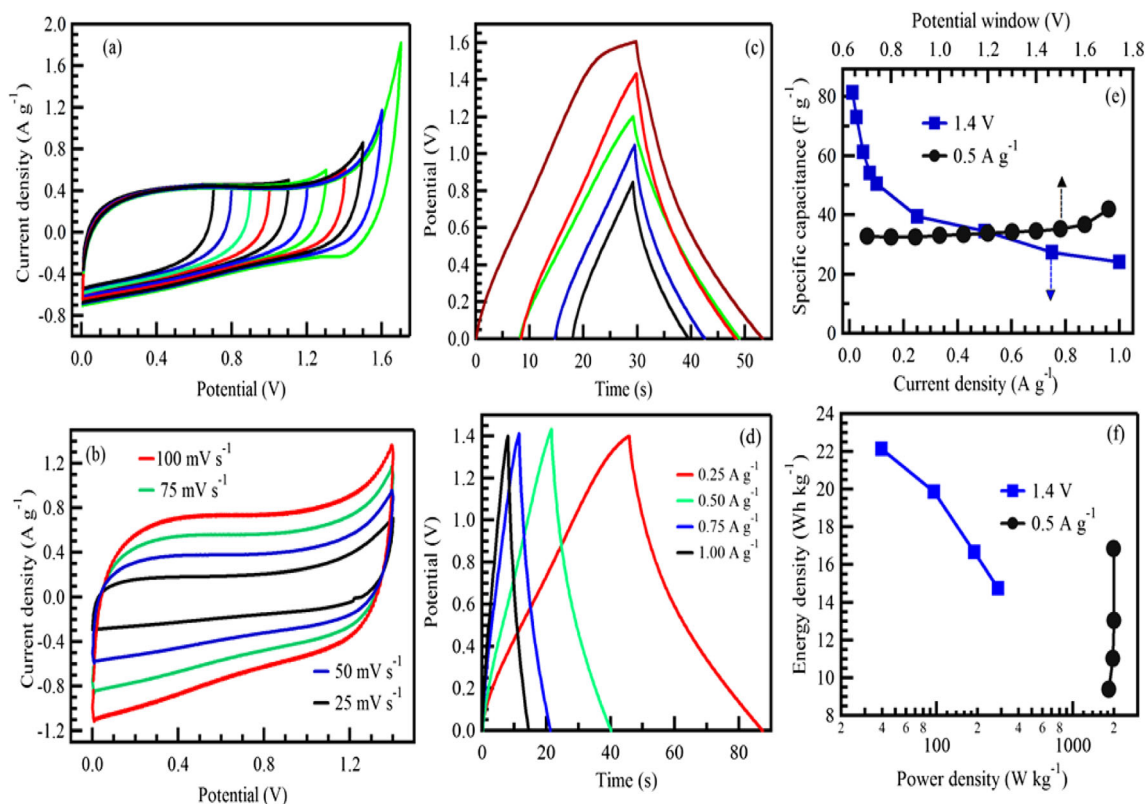

Fig. 10 Cyclic voltammetry curves under different potential windows at 50 mV s^{-1} (**a**) at different scan rates in potential windows of 0–1.4 V (**b**), galvanostatic charge/discharge curves at 0.5 A g^{-1} under different potential windows (**d**), at different current densities under 1.4 V (**d**), specific capacitance as a function of current density and potential window (**e**), and Ragone plots (**f**) for S3//S3 symmetric supercapacitor in 3 M KOH

Fig. 11 Capacitance retention (left vs. bottom) and coulombic efficiency (right vs. bottom) of S3//S3 at 0.5 A g^{-1} (insets show the charge/discharge of the 1st and 4500th cycles)
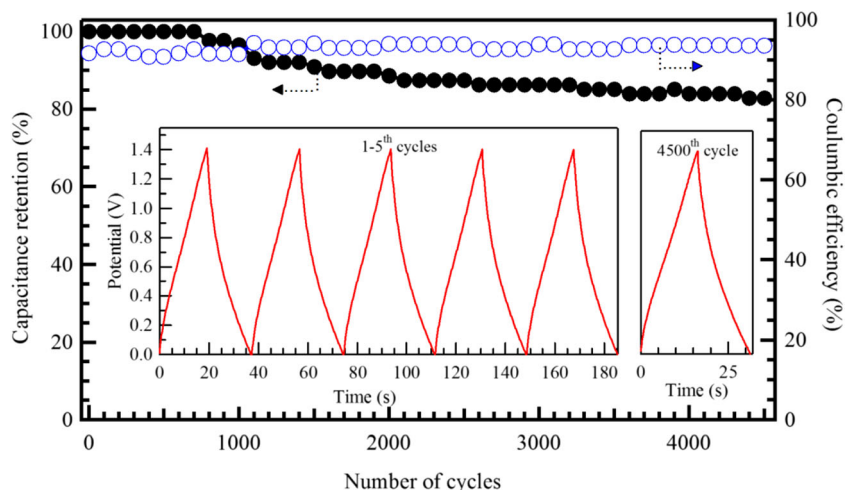
biomass-derived nitrogen-doped carbons (13.0 Wh kg^{-1}) [38], straw-based porous carbon fibers (16.0 Wh kg^{-1}) [56], and peach gum-derived porous carbon nanosheets (17.3 Wh kg^{-1}) [57].

The cycling stability of S3//S3 was performed using galvanostatic charge/discharge at 0.5 A g^{-1} for 4500 cycles and the data are presented as shown in Fig. 11. S3//S3 showed very good cycling stability where it still maintained more than 78% of its original capacitance in KOH. Moreover, it shows the high coulombic efficiency of 90%. This is due to easily insertion–desertion of the electrolyte ions through the porous carbon structure [15]. Some galvanostatic charge/discharge cycles are shown as insets of Fig. 11 to confirm stable and uniform performance.

4 Conclusions

Oxygen self-doped carbon nanospheres were successfully obtained from *Allium cepa* peel as a biowaste precursor. The obtained electrochemical behavior in 3 M KOH showed excellent supercapacitance performance (189.4 at 0.1 A g^{-1}) of the prepared carbon nanospheres electrode. Impedance spectra showed a low resistivity of carbon nanospheres, supporting its suitability for supercapacitor electrodes application. That is due to their fine particles size of ~ 60 nm and porous structure. The full supercapacitor device fabricated from carbon nanospheres showed the high cyclic stability of about 78% and high coulombic efficiency of 90% over 4500 cycles at 0.5 A g^{-1}. The symmetric supercapacitor shows a good electrochemical performance in KOH up to 1.7 V, with a high energy density of 22.1 Wh kg^{-1}. The obtained results recommend these carbon nanospheres obtained from *Allium cepa* wastes for supercapacitor applications.

References

1. Lefèvre M, Proietti E, Jaouen F, Dodelet J-P (2009) Iron-based catalysts with improved oxygen reduction activity in polymer electrolyte fuel cells. Science 324(5923):71–74
2. Yan J, Wang Q, Wei T, Fan Z (2014) Recent advances in design and fabrication of electrochemical supercapacitors with high energy densities. Adv Energy Mater 4(4):1300816
3. Zhang LL, Zhao X (2009) Carbon-based materials as supercapacitor electrodes. Chem Soc Rev 38(9):2520–2531
4. Thalji MR, Ali GAM, Algarni H, Chong KF (2019) Al^{3+} ion intercalation pseudocapacitance study of W$_{18}$O$_{49}$ nanostructure. J Power Sources 438:227028
5. Pech D, Brunet M, Durou H, Huang P, Mochalin V, Gogotsi Y, Taberna P-L, Simon P (2010) Ultrahigh-power micrometre-sized supercapacitors based on onion-like carbon. Nat Nanotechnol 5(9):651
6. Yu Z, Tetard L, Zhai L, Thomas J (2015) Supercapacitor electrode materials: nanostructures from 0 to 3 dimensions. Energy Environ Sci 8(3):702–730
7. Ali GAM, Lih Teo EY, Aboelazm EAA, Sadegh H, Memar AOH, Shahryari-Ghoshekandi R, Chong KF (2017) Capacitive performance of cysteamine functionalized carbon nanotubes. Mater Chem Phys 197:100–104
8. Ali GAM, Divyashree A, Supriya S, Chong KF, Ethiraj AS, Reddy MV, Algarni H, Hegde G (2017) Carbon nanospheres derived from Lablab purpureus for high performance supercapacitor electrodes: a green approach. Dalton Trans 46(40):14034–14044
9. Ali GAM, Abdul Manaf SA, Kumar A, Chong KF, Hegde G (2014) High performance supercapacitor using catalysis free porous carbon nanoparticles. J Phys D Appl Phys 47(49):495307–495313

10. Yuan C, Gao B, Shen L, Yang S, Hao L, Lu X, Zhang F, Zhang L, Zhang X (2011) Hierarchically structured carbon-based composites: design, synthesis and their application in electrochemical capacitors. Nanoscale 3(2):529–545

11. Hegde G, Abdul Manaf SA, Kumar A, Ali GAM, Chong KF, Ngaini Z, Sharma KV (2015) Biowaste sago bark based catalyst free carbon nanospheres: waste to wealth approach. ACS Sustain Chem Eng 5(9):2247–2253

12. Ali GAM, Habeeb OA, Algarni H, Chong KF (2018) CaO impregnated highly porous honeycomb activated carbon from agriculture waste: symmetrical supercapacitor study. J Mater Sci

13. Supriya S, Shetti VS, Hegde G (2018) Conjugated system of porphyrin-carbon nano allotropes: a review. New J Chem

14. Jiang H, Lee PS, Li C (2013) 3D carbon based nanostructures for advanced supercapacitors. Energy Environ Sci 6(1):41–53

15. Chen T, Dai L (2013) Carbon nanomaterials for high–performance supercapacitors. Mater Today 16(7–8):272–280

16. Ali GAM, Makhlouf SA, Yusoff MM, Chong KF (2015) Structural and electrochemical characteristics of graphene nanosheets as supercapacitor electrodes. Rev Adv Mater Sci 40(1):35–43

17. Ali GAM, Megiel E, Romański J, Algarni H, Chong KF (2018) A wide potential window symmetric supercapacitor by TEMPO functionalized MWCNTs. J Mol Liq 271:31–39

18. Teo EYL, Muniandy L, Ng E-P, Adam F, Mohamed AR, Jose R, Chong KF (2016) High surface area activated carbon from rice husk as a high performance supercapacitor electrode. Electrochim Acta 192:110–119

19. Wang H, Li Z, Tak JK, Holt CM, Tan X, Xu Z, Amirkhiz BS, Harfield D, Anyia A, Stephenson T (2013) Supercapacitors based on carbons with tuned porosity derived from paper pulp mill sludge biowaste. Carbon 57:317–328

20. Long C, Chen X, Jiang L, Zhi L, Fan Z (2015) Porous layer-stacking carbon derived from in-built template in biomass for high volumetric performance supercapacitors. Nano Energy 12:141–151

21. Gao S, Li L, Geng K, Wei X, Zhang S (2015) Recycling the biowaste to produce nitrogen and sulfur self-doped porous carbon as an efficient catalyst for oxygen reduction reaction. Nano Energy 16:408–418

22. Yan L, Yu J, Houston J, Flores N, Luo H (2017) Biomass derived porous nitrogen doped carbon for electrochemical devices. Green Energy Environ 2(2):84–99

23. Gao Z, Huang X, Kuiyong C, Wan C, Liu H (2017) Heteroatom-enhanced the formation of mesoporous carbon microspheres with high surface area as supercapacitor electrode materials. Int J Electrochem Sci 12(11):10687–10700

24. Raymundo-Piñero E, Leroux F, Béguin F (2006) A high-performance carbon for supercapacitors obtained by carbonization of a seaweed biopolymer. Adv Mater 18(14):1877–1882

25. Shakambari G, Sameer Kumar R, Ashokkumar B, Varalakshmi P (2017) Agro waste utilization for cost-effective production of l-asparaginase by pseudomonas plecoglossicida RS1 with anticancer and acrylamide mitigation potential. ACS Omega 2(11):8108–8117

26. Benítez V, Mollá E, Martín-Cabrejas MA, Aguilera Y, López-Andréu FJ, Cools K, Terry LA, Esteban RM (2011) Characterization of industrial onion wastes (Allium cepa L.): dietary fibre and bioactive compounds. Plant foods Hum Nutr 66(1):48–57

27. Aruni Abdul Manaf S, Hegde G, Kumar Mandal U, Tin Wui W, Roy P (2017) Functionalized carbon nano-scale drug delivery systems from biowaste sago bark for cancer cell imaging. Curr Drug Deliv 14(8):1071–1077

28. Yallappa S, Manaf SAA, Hegde G (2018) Synthesis of a biocompatible nanoporous carbon and its conjugation with florescent dye for cellular imaging and targeted drug delivery to cancer cells. New Carbon Mater 33(2):162–172

29. Yallappa S, Manaf SAA, Shiddiky MJ, Kim JH, Hossain M, Shahriar A, Malgras V, Yamauchi Y, Hegde G (2017) Synthesis of carbon nanospheres through carbonization of areca nut. J Nanosci Nanotechnol 17(4):2837–2842

30. Yallappa S, Shivakumar M, Nagashree K, Dharmaprakash M, Vinu A, Hegde G (2018) Electrochemical determination of nitrite using catalyst free mesoporous carbon nanoparticles from bio renewable areca nut seeds. J Electrochem Soc 165(10):H614–H619

31. Divyashree A, Manaf SAA, Yallappa S, Chaitra K, Kathyayini N, Hegde G (2016) Low cost, high performance supercapacitor electrode using coconut wastes: eco-friendly approach. J Energy Chem 25(5):880–887

32. Carrott P, Carrott MR, Guerrero C, Delgado L (2008) Reactivity and porosity development during pyrolysis and physical activation in CO2 or steam of kraft and hydrolytic lignins. J Anal Appl Pyrolysis 82(2):264–271

33. Ferrari AC, Basko DM (2013) Raman spectroscopy as a versatile tool for studying the properties of graphene. Nat Nanotechnol 8(4):235

34. Akshaya K, Bhat VS, Varghese A, George L, Hegde G (2019) Non-enzymatic electrochemical determination of progesterone using carbon nanospheres from onion peels coated on carbon fiber paper. J Electrochem Soc 166(13):B1097–B1106

35. Contreras E, Dominguez D, Tiznado H, Guerrero-Sanchez J, Takeuchi N, Alonso-Nunez G, Contreras OE, Oropeza-Guzmán MT, Romo-Herrera JM (2019) N-Doped carbon nanotubes enriched with graphitic nitrogen in a buckypaper configuration as efficient 3D electrodes for oxygen reduction to H_2O_2. Nanoscale 11(6):2829–2839

36. Thommes M, Kaneko K, Neimark AV, Olivier JP, Rodriguez-Reinoso F, Rouquerol J, Sing KS (2015) Physisorption of gases, with special reference to the evaluation of surface area and pore size distribution (IUPAC Technical Report). Pure Appl Chem 87(9-10):1051–1069

37. Fouad OA, Makhlouf SA, Ali GAM, El-Sayed AY (2011) Cobalt/silica nanocomposite via thermal calcination-reduction of gel precursors. Mater Chem Phys 128(1):70–76

38. Yu D, Ma Y, Chen M, Dong X (2019) KOH activation of wax gourd-derived carbon materials with high porosity and heteroatom content for aqueous or all-solid-state supercapacitors. J Colloid Interface Sci 537:569–578

39. Zhang J, Gong L, Sun K, Jiang J, Zhang X (2012) Preparation of activated carbon from waste Camellia oleifera shell for supercapacitor application. J Solid State Electrochem 16(6):2179–2186

40. Ali GAM, Yusoff MM, Shaaban ER, Chong KF (2017) High performance MnO_2 nanoflower supercapacitor electrode by electrochemical recycling of spent batteries. Ceram Int 43:8440–8448

41. Kumar A, Hegde G, Manaf SA, Ngaini Z, Sharma KV (2014) Catalyst free silica templated porous carbon nanoparticles from bio–waste materials. Chem Commun 50(84):12702–12705

42. Hulicova D, Yamashita J, Soneda Y, Hatori H, Kodama M (2005) Supercapacitors prepared from melamine-based carbon. Chem Mater 17(5):1241–1247

43. Barzegar F, Momodu DY, Fashedemi OO, Bello A, Dangbegnon JK, Manyala N (2015) Investigation of different aqueous electrolytes on the electrochemical performance of activated carbon-based supercapacitors. RSC Adv 5(130):107482–107487

44. Chen M, Zheng X, Ma Y, Dong X (2018) Oxygen-rich porous carbon sheets: facile one-step synthesis and enhanced electrochemical performance. Diam Relat Mater 85:89–97

45. Si W, Wu X, Zhou J, Guo F, Zhuo S, Cui H, Xing W (2013) Reduced graphene oxide aerogel with high–rate supercapacitive performance in aqueous electrolytes. Nanoscale Res Lett 8(1):247–255

46. Wu F-C, Tseng R-L, Hu C-C, Wang C-C (2005) Effects of pore structure and electrolyte on the capacitive characteristics of steam-

and KOH-activated carbons for supercapacitors. J Power Sources 144(1):302–309

47. Ahmed S, Ahmed A, Rafat M (2018) Supercapacitor performance of activated carbon derived from rotten carrot in aqueous, organic and ionic liquid based electrolytes, Journal of Saudi Chemical Society

48. Portet C, Taberna PL, Simon P, Flahaut E, Laberty-Robert C (2005) High power density electrodes for carbon supercapacitor applications. Electrochim Acta 50(20):4174–4181

49. Zequine C, Ranaweera CK, Wang Z, Dvornic PR, Kahol PK, Singh S, Tripathi P, Srivastava ON, Singh S, Gupta BK, Gupta G, Gupta RK (2017) High-performance flexible supercapacitors obtained via recycled jute: bio-waste to energy storage approach. Sci Rep 7:1174

50. Subramanian V, Luo C, Stephan AM, Nahm KS, Thomas S, Wei B (2007) Supercapacitors from activated carbon derived from banana fibers. J Phys Chem C 111(20):7527–7531

51. Aboelazm EAA, Ali GAM, Algarni H, Yin H, Zhong YL, Chong KF (2018) Magnetic electrodeposition of the hierarchical cobalt oxide nanostructure from spent lithium-ion batteries: its application as a supercapacitor electrode. J Phys Chem C 122(23):12200–12206

52. Ali GAM, Manaf SAA, Divyashree A, Chong KF, Hegde G (2016) Superior supercapacitive performance in porous nanocarbons. Journal of Energy Chemistry 25(4):734–739

53. Kant R, Kaur J, Singh MB (2014) Chapter 10 Nanoelectrochemistry in India, Electrochemistry. The Royal Society of Chemistry 12:336–378

54. Balathanigaimani M, Shim W-G, Lee M-J, Kim C, Lee J-W, Moon H (2008) Highly porous electrodes from novel corn grains-based activated carbons for electrical double layer capacitors. Electrochem Commun 10(6):868–871

55. Chen M, Yu D, Zheng X, Dong X (2019) Biomass based N-doped hierarchical porous carbon nanosheets for all-solid-state supercapacitors. J Energy Storage 21:105–112

56. Zheng X, Chen M, Ma Y, Dong X, Xi F, Liu J (2017) Enhanced electrochemical performance of straw-based porous carbon fibers for supercapacitor. J Solid State Electrochem 21(12):3449–3458

57. Ma Y, Chen M, Zheng X, Yu D, Dong X (2019) Synergetic effect of swelling and chemical blowing to develop peach gum derived nitrogen-doped porous carbon nanosheets for symmetric supercapacitors. J Taiwan Inst Chem Eng 101:24–30

Affiliations

Gomaa A. M. Ali[1,2] · S. Supriya[3,4] · Kwok Feng Chong[1] · Essam R. Shaaban[5] · H. Algarni[6,7] · T. Maiyalagan[8] · Gurumurthy Hegde[3]

[1] Faculty of Industrial Sciences & Technology, Universiti Malaysia Pahang, Gambang, 26300 Kuantan, Malaysia

[2] Chemistry Department, Faculty of Science, Al–Azhar University, Assiut 71524, Egypt

[3] Centre for Nano-Materials and Displays, B.M.S. College of Engineering, Bull Temple Road, Bangalore 560019, India

[4] Department of Chemistry, B.M.S. College of Engineering, Bull Temple Road, Bangalore 560019, India

[5] Physics Department, Faculty of Science, Al-Azhar University, Assiut 71524, Egypt

[6] Department of Physics, Faculty of Sciences, King Khalid University, P.O. Box 9004, Abha, Saudi Arabia

[7] Research Center for Advanced Materials Science (RCAMS), King Khalid University, P.O. Box 9004, Abha 61413, Saudi Arabia

[8] Department of Chemistry, SRM Institute of Science and Technology, Kattankulathur 603203, India